metals

MDPI

Article

Corrosion Behaviour of L80 Steel Grade in Geothermal Power Plants in Switzerland

Ana Vallejo Vitaller [1,*], Ueli M. Angst [1] and Bernhard Elsener [1,2]

[1] Institute for Building Materials (IfB), ETH Zurich, Stefano-Franscini-Platz 3, 8093 Zurich, Switzerland; ueli.angst@ifb.baug.ethz.ch (U.M.A.); elsener@ifb.baug.ethz.ch (B.E.)

[2] Department of Chemical and Geological Sciences, University of Cagliari, 09100 Monserrato (CA), Italy

* Correspondence: ana.vallejo@ethz.ch; Tel.: +41-44-633-2786

Received: 20 January 2019; Accepted: 7 March 2019; Published: 15 March 2019

Abstract: In Switzerland, deep geothermal energy can give a promising contribution to the future energy scenario. However, the expertise in operational issues of deep geothermal power plants is limited, and technical challenges, such as corrosion, are a determining factor for their reliable and long-term operation. In this work, two representative fluids of optimal geothermal conditions in Switzerland were studied. The corrosiveness of the solutions was assessed using two experimental setups that allow investigating the range of temperatures and pressures that apply to the reservoir and power plant conditions. The corrosion behaviour of API L80 steel was analyzed by means of electrochemical measurements (at 100 and 200 °C) and of gravimetric tests (at 100 °C). After the tests, the morphologies and composition of the corrosion products were obtained by scanning electron microscopy (SEM) coupled with energy dispersive X-Ray (EDX) and X-Ray diffraction (XRD). Results show that corrosion rates are significantly high at 100 °C in environments with a chloride concentration of around 600 mg/L and pH around 7. The corrosion products deposited on the metal surface mainly consist of magnetite and/or hematite that might potentially form a protective layer. This study gives a first insight of the potential corrosiveness of geothermal fluids in Switzerland.

Keywords: deep geothermal energy; operational issues; materials degradation; carbon steel; autoclave; electrochemistry

1. Introduction

The sustainable use of geothermal resources shows significant potential worldwide for the generation of electricity and/or direct heat [1,2]. In comparison to other renewable energies as, for example, wind power or photovoltaics, geothermal energy presents many advantages, such as high thermal efficiency, cost-effectiveness, and permanent availability [3–6]. In this context, the Swiss Federal Office of Energy approved in 2011 an ambitious "Energy strategy 2050" focusing on sustainable and renewable electricity production [7]. This will require around 4–5 TWh/year from deep geothermal resources by 2050, representing approximately 7.5% of the expected annual power need [8].

Petrothermal systems, also commonly known as engineered or enhanced geothermal systems (EGS), represent the most suitable and efficient technology for generating electricity [9]. In Switzerland, they might significantly contribute to its energy mix [10,11], due to the existing geothermal conditions underneath a large area of the country. These refer to low-permeability rocks at temperatures of 160–200 °C, located at depths between 3 km and 6 km and mostly in the crystalline basement [11,12]. The development of this technology, however, faces relevant challenges: (i) accessibility (namely, drilling) [13–16]; (ii) reservoir creation (namely, hydraulic fracturing and triggered seismicity) [17–19]; and (iii) long-term durability (namely, materials degradation due to corrosion and scaling) [20–23]. In this regard, the choice of corrosion-resistant, yet economically affordable materials is crucial to

maintain the facilities in service, assuming a plant's lifetime of 30 years [24,25]. This selection is based on aspects that concern the knowledge of physical and chemical properties of deep geothermal fluids and their long-term interaction with metallic components [26].

As of today, no electrical energy from deep geothermal resources is yet produced in Switzerland [10,11,27]. This results in a limited knowledge about properties of deep geothermal fluids (at depths of 4–5 km) [10] and, thus, a lack of expertise in corrosion issues of geothermal installations. Furthermore, literature on corrosion shows that most of the experimental studies are restricted to specific geothermal fields [23,28–32]. Considering that the fluid chemistry might significantly vary not only between physically separated fields but also between nearby boreholes [33,34], the transfer of technical know-how of existing geothermal power plants abroad to design durable, maintenance-free facilities in Switzerland constitutes a research challenge.

This paper aims at characterizing the corrosiveness of geothermal fluids that are most favourable for the production of electricity in Switzerland. As a first step towards a better understanding of hydrochemistry-related issues, geothermal environments that may be optimal for electricity generation were identified. In these conditions, the corrosion resistance of inexpensive materials was evaluated in an experimental setup that mimics the harsh conditions occurring in deep geothermal systems (high temperature, high pressure). The results from this work will pave the way to the development of future geothermal power plants in Switzerland by providing guidelines for the selection of materials that can reach the required long-term durability.

1.1. Corrosion in Binary Geothermal Power Plants

EGS present reservoirs of low-porosity and low-permeability and with little water in-place (Figure 1) [35]. However, the permeability of the reservoir and, thus, the productivity of the well may be increased by means of hydraulic fracturing [13,14]. Although low-salinity water is generally injected at high pressure and low temperature into the crystalline reservoir, the fluid interacts with the rocks therein, resulting in heat transfer and subsequent dissolution of minerals, salts, and gases [36]. While the fluid might reach temperatures of around 200 °C in the reservoir in low- to medium-enthalpy water-dominated systems, the temperature at the binary power plant on the surface might decrease down to 100 °C [37]. In operating binary power plants, the pressure is usually increased at the wellhead by means of downhole pumps as a measure to prevent scaling formation. For instance, at the geothermal power plant of Soultz-sous-Forêts, the pump is used to maintain a pressure of around 20 bar in the surface installation [38].

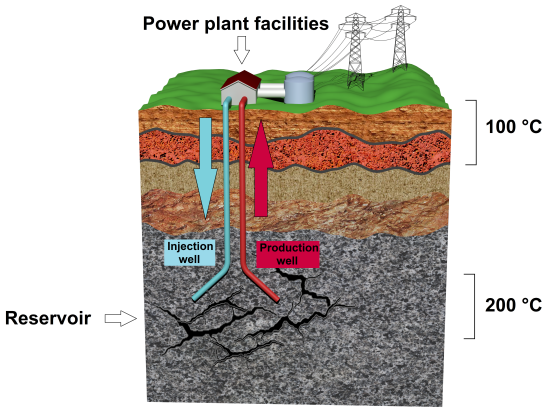

Figure 1. Scheme of a deep geothermal energy system. The power plant on the surface, the reservoir at a depth of 4–5 km, and the injection and production wells are indicated. The temperature of the fluid varies through the cycle from 200 °C in the reservoir down to 100 °C on the surface.

As shown in Figure 1, the fluid circulates in a cycle through wells, pipelines, downhole pumps, and heat exchangers. These components are subject to premature deterioration, since they are

mostly made of metals and alloys that are exposed to brines at high temperatures [39]. Therefore, deep geothermal energy is not free of technical problems, being that corrosion is a major hazard for the reliable and long-term operation of geothermal power plants [40]. The most common types of corrosion are uniform, pitting, and crevice corrosion [41]. In bicarbonate environments with very low chloride concentrations, low-alloyed carbon steels show noticeable resistance to uniform corrosion [32]. However, environments with high chloride concentrations and low pH (around 6) might lead to uniform attack and to the formation of pits on the steel surface [28–30]. Other brines containing non-condensable gases, such as H_2S, are very aggressive for this type of steels, resulting in significantly high corrosion rates [23,30,31].

1.2. Representative Swiss Geothermal Fluids

The geothermal fluids tested in this work represent ideal conditions for the production of geothermal energy in Switzerland. These fluids were preliminarily selected from a database reported by Sonney and Vuataz [42]. The authors present the physical, chemical, and hydrogeological properties of 203 fluids sampled from springs and boreholes in 82 different locations in Switzerland and neighbouring countries.

Here, the geothermal fluids were selected on the basis of three key parameters: geographical location, reservoir formation, and geothermal gradient. In regard to location, the fluids were sampled from well boreholes located in the northern part of Switzerland (Figure 2). This is an area of great interest for geothermal energy purposes, as the heat flow therein is considerably high in comparison to the Swiss average and the temperatures at 5 km depth are estimated to be above 190 °C ([10,43] and references therein). The fluids also come from reservoirs lying in the crystalline granitic basement, which is usually the target formation for the EGS technology [44]. In addition, the geothermal gradients in these well boreholes are above 30 °C/km. Six representative fluids served as reference cases for our study and mainly differ in pH (6.5 to 8.8) and concentration of chlorides (25 to 3555 mg/L). The chemical composition of the selected geothermal fluids is shown in Table 1.

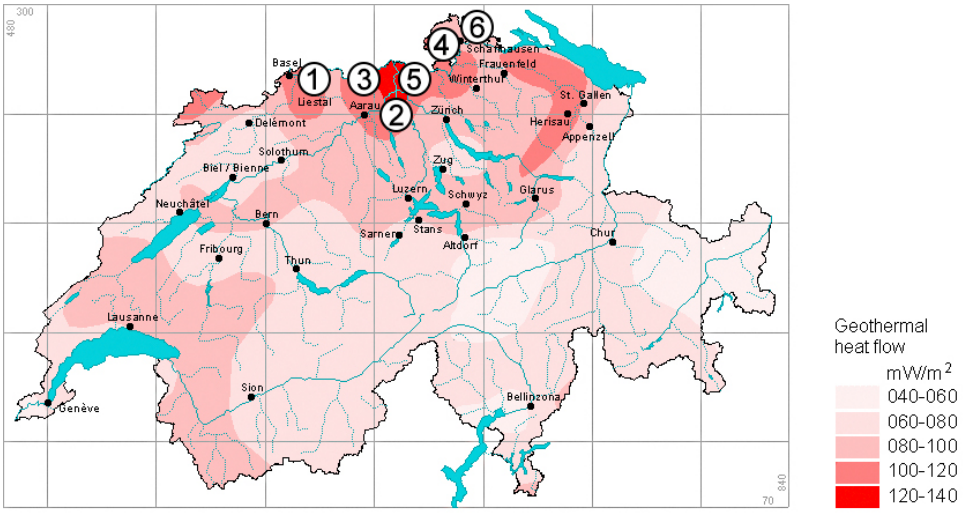

Figure 2. Map of the geothermal heat flow in Switzerland showing the sampling location of the selected geothermal fluids (1–6) in the Northern part of Switzerland that has the largest potential for deep geothermal energy production, adapted from (ref. [45], cartographic mapped by Energie-Atlas GmbH (Switzerland, 2004)).

Table 1. Chemical composition of six selected fluids (Figure 2) representative for the Northern part of Switzerland. The concentration of the chemical species is in mg/L, adapted from ref. [46].

Fluid	pH	Temp (°C)	Ca^{2+}	Mg^{2+}	Na^{+}	K^{+}	HCO_3^{-}	SO_4^{2-}	Cl^{-}
1	6.50	25.8	260.0	45.6	856.0	35.0	1423.0	950.0	556.0
2	6.78	30.7	88.0	21.0	2712.0	168.0	891.0	793.0	3555.0
3	7.93	34.9	34.1	3.0	363.5	24.2	366.0	532.0	73.1
4	8.2	57	5.5	0.4	172.1	4.6	281.0	64.0	27.0
5	8.25	31.3	8.5	0.2	395.4	8.3	372.0	339.0	142.0
6	8.8	47	6.0	0.7	172.1	3.8	267.0	71.0	25.0

2. Materials and Methods

2.1. Synthetic Geothermal Fluids

On the basis of the chemical composition of the six fluids (Table 1), we designed two synthetic testing solutions. The first one had a chemical composition similar to the average one of solutions 4–6, with an alkaline pH and being chloride-free (solution A in Table 2). The second one, on the other side, had a chemical composition similar to the average concentration of the ions of solutions 1–3, with a resulting nearly neutral pH and high chloride concentration (solution B in Table 2). The fluids were prepared by mixing specific quantities of different stock solutions with ultrapure water at room temperature. Sodium bicarbonate (ACS, Reag. pH Eur) and sodium chloride (ACS, ISO, Reg. Ph Eur for analysis) were purchased from Merck (Merck KGaA, Darmstadt, Germany) and hydrochloric acid (37%, Reag. Ph. Eur. analytical reagent) from VWR Chemicals. The rest of the chemicals (calcium sulfate (99%), sodium sulfate (>99.0%), potassium sulfate (>99.0%), and magnesium sulfate (>99.5%)) were purchased from Sigma-Aldrich GmbH (Buchs, Switzerland). The resulting chemical composition of the synthetic fluids is presented in Table 2.

Table 2. Chemical composition of the selected fluids as prepared in the laboratory at room temperature. The concentration of the chemical species is in mg/L. The pH values reported here were measured at room temperature immediately after the preparation of the solutions.

Fluid	pH	Ca^{2+}	Mg^{2+}	Na^{+}	K^{+}	HCO_3^{-}	SO_4^{2-}	Cl^{-}
A	8.4–9.0	10.0	-	282.8	-	399.8	300.0	-
B	6.5–7.4	250.0	45.0	747.0	35.0	1400.0	900.0	600.0

2.2. Materials

A low-alloyed steel, L80 type 1, was used in all experiments. This steel grade is commonly used for the tubing and casing of wells and is commercially manufactured according to the specification 5CT of the American Petroleum Institute (API) [47]. It has a tempered martensitic microstructure and a tensile strength of minimum 550 MPa (80 ksi). The chemical composition of this material is shown in Table 3.

Table 3. Chemical composition of the steel grade API L80 type 1, as analyzed by the producer from a batch of liquid steel.

Steel Sample	wt.% (and Fe bal.)										
Composition	C	Si	Mn	Cr	Mo	S	P	Ni	Cu	Al	V
L80 Type 1	0.25	0.19	1.02	0.45	0.16	0.004	0.014	0.04	0.02	0.03	0.003

The test specimens were machined from a pipe into two different shapes and sizes: a cylinder type (20 mm height and 15 mm diameter) for electrochemical measurements (Figure 3a) and a disc type (3 mm thickness and 15 mm diameter and a hole of around 7 mm diameter) for gravimetric tests

(Figure 3b). In these Figures, it can be noticed that the surface area of both types of metal coupons in contact with the sample holder has been minimized in order to avoid crevice corrosion. The surface areas of the specimens exposed to the testing fluids were 1119 mm^2 (cylinders) and 484 mm^2 (discs). All exposed surfaces were mechanically ground and/or polished: (i) horizontal surface of cylinders manually ground in ethanol using SiC abrasive paper (up to 1200 mesh/in) and polished using diamond suspensions of 1, 3, and 6 µm; (ii) longitudinal surface of cylinders manually ground in ethanol with SiC paper (up to 4000 mesh/in); (iii) all surfaces of discs manually ground in ethanol with SiC paper (up to 4000 mesh/in). After the surfaces preparation, all the samples were ultrasonically cleaned with ethanol and dried with compressed air.

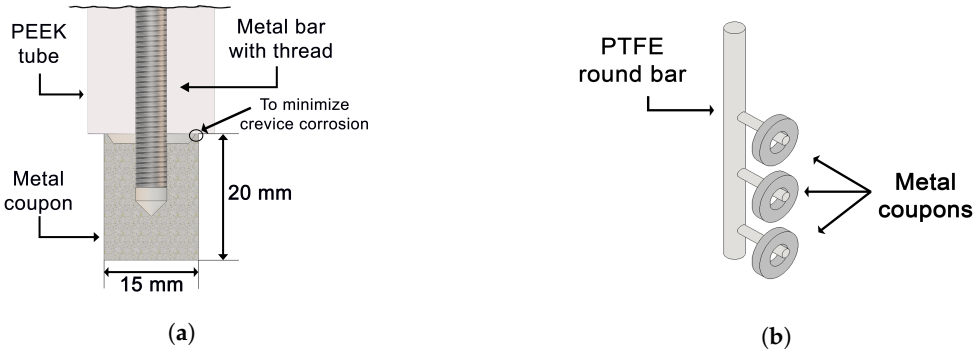

Figure 3. Types of supporting devices used in the setups for the electrochemical and gravimetric tests. (**a**) Sample holder with a poly(ether-ether-ketone) PEEK tube and a screwed metal bar, where the metal coupon is attached; (**b**) sample holder with a polytetrafluoroethylene (PTFE) bar where the metal coupons are mounted.

2.3. Experimental Procedures

Two types of experiments were carried out to evaluate the corrosion behaviour of metal samples in geothermal environments. First, electrochemical tests were performed in a cell suitable for high temperatures and high pressures, where cylindrical coupons (Figure 3a) were used. Additionally, gravimetric experiments were carried out for a duration of around 30 days in glass round-bottom flasks at 90–100 °C, where discs coupons (Figure 3b) were tested.

2.3.1. Electrochemical Measurements at High Temperature and Pressure

A set of experiments was performed in an experimental setup at 100 and 200 °C to simulate the conditions found in the power plant facilities above ground (namely, in the heat exchangers and piping system), and in the boreholes, respectively. The setup was composed of an autoclave constructed with a durable material that resists to these conditions and to the corrosive environment of the geothermal fluid. The setup also allowed us to perform electrochemical corrosion tests by using a three-electrode configuration. The experimental setup used for the tests is illustrated in detail elsewhere [48].

For the experiments, the oxygen concentration in the fluid was significantly reduced by de-aerating the solution with nitrogen (purity grade 5.0) for 60 min prior to the start of the tests. In order to prevent degassing of the solution when the temperature rose, nitrogen was initially injected into the vessel at a pressure of 15 bar. The magnetic stirrer was set at a constant speed of 500 rpm, except during the electrochemical measurements. The duration of each single experiment was 120 h at the target temperature of either 100 or 200 °C. The heating and cooling rates were 50 °C/h.

Electrochemical measurements were performed using a potentiostat/galvanostat PGSTAT302N by Metrohm Autolab B.V. (Utrecht, The Netherlands), operated by the Windows software NOVA 2.1.2 (also by Metrohm Autolab). In addition, a Keithley multimeter (model 2701) and a multiplexer (model 7702), connected to a computer for data acquisition, continuously and simultaneously recorded the potential of the working electrode (i.e., the open circuit potential, OCP) and of the pH sensor against a

reference electrode. The latter was a silver chloride (Ag/AgCl) electrode suitable for testing conditions of high temperature and pressure.

The corrosion status of the metallic material was evaluated and investigated by electroanalytical techniques. One of the most used techniques to accurately determine corrosion rates is the linear polarization resistance (LPR) method [49,50]. A very small external DC overvoltage (around 10–20 mV from the OCP) was applied to the working electrode. In this situation, the current flowing from the counter electrode to the working electrode was recorded. According to Stern and Geary [49], the corrosion current density (i_{corr}) was calculated as

$$i_{corr} = \frac{B}{R_p} = \frac{1}{2.303 \cdot \left(\frac{1}{\beta_a} + \frac{1}{|\beta_b|}\right)} \cdot \frac{1}{R_p}, \quad (1)$$

where i_{corr} is the corrosion current density (A/cm^2), B is the constant (V), R_p the polarization resistance ($\Omega \cdot$cm^2), and β_a and β_b are the anodic and cathodic Tafel slopes, respectively. It is assumed that both Tafel slopes are $\pm$ 0.12 V [51]. Considering Equation (1) and Faraday's first law of electrolysis, the corrosion rate (mm/year) of a metal (e.g., steel) can be determined as

$$\text{Corrosion rate} = K \cdot \frac{i_{corr} \cdot M_{Fe}}{z \cdot F \cdot \rho_{Fe}}, \quad (2)$$

where K is a constant (3.15×10^8), F is the Faraday constant (96,485 C/mol) and M_{Fe} (g/mol), ρ_{Fe} (g/cm^3), and z indicate the molar mass, density, and oxidation state of iron, respectively.

2.3.2. Gravimetric Experiments

Gravimetric experiments were carried out according to the ASTM standard G31-12a [52]. Metal coupons were first exposed to fluids A and B at around 100 °C in two different 1 L round-bottom flasks that included reflux condensers, spargers for aeration, and resistance thermometers (Pt100). These coupons were loosely mounted on polytetrafluoroethylene (PTFE) bars to minimize crevice corrosion. Prior to the start, the fluids were deareated with nitrogen (purity grade 5.0) for around 1 h. The flasks were then immersed in silicone oil baths and the temperature controlled at 100 °C by a heating plate that incorporated stirring function. The duration of the tests was around 720 h (i.e., 30 days).

After exposure, the metal coupons were removed from the flasks and chemically cleaned. The procedure for removing the corrosion products followed the ASTM standard G1-03 [53]. The metal coupons were immersed in a solution of 500 mL concentrated hydrochloric acid, 3.5 g hexamethylene tetramine and ultrapure water (up to 1 L) for 10 min at room temperature. Chemical cleaning was followed by ultrasonic cleaning in ultrapure water to remove any remaining corrosion product and samples were weighed in a NewClassic MF analytical balance by Mettler Toledo (Greifensee, Switzerland). The average corrosion rate (time average) in mm/year was obtained for each specimen with the following equation

$$\text{Corrosion rate} = K' \cdot \frac{m_{loss}}{A \cdot t \cdot \rho_{Fe}}, \quad (3)$$

where K' is a constant (8.76×10^4), m_{loss} is the mass loss (g), A is the exposed area (cm^2), t is the exposure time (h), and ρ_{Fe} is the density of iron (g/cm^3).

2.3.3. Analysis Post-Exposure

Corrosion products deposited on the surface of the metal samples were analyzed by a number of analytical techniques, such as stereomicroscopy, scanning electron microscopy (SEM) coupled with energy dispersive X-Ray (EDX) spectroscopy, and X-Ray diffraction (XRD). The used SEM was a FEI Quanta 200 3D (FEI, NorthAmerica NanoPort, Hillsboro, OR, USA), the EDX was a Genesis 4000 by

EDAX (Mahwah, NJ, USA), and the used XRD was a Bruker D8 Advanced diffractometer (Bruker AXS GmbH, Karlsruhe, Germany). Secondary electron (SE)-images were obtained in a high vacuum mode from samples that were covered previously with a carbon coating of 5–10 nm thickness. The operating voltage was 10 kV. In addition, the compositional changes of the synthetic fluids were assessed via inductively coupled plasma optical emission spectroscopy (ICP-OES). A Thermo Scientific iCAP 6300 Dual View ICP-OES (Thermo Fisher Scientific Inc., Waltham, MA, USA) with a CETAC ASX-260 autosampler (CETAC, Omaha, NE, USA) was used for the analyses.

3. Results

3.1. pH Evolution

Figure 4 shows the pH values that were measured in the autoclave while testing fluid A and B. This Figure shows three regions that correspond to the heating phase (from 90 °C up to either 100 or 200 °C), the test phase of five days at the target temperature assigned for electrochemical measurements, and, lastly, the cooling phase (down to 90 °C). The pH slightly changed over time in all of the tested combinations of fluids and temperatures. Furthermore, the pH was measured at room temperature before and after each experiment, indicating a variation of less than 0.7 pH units.

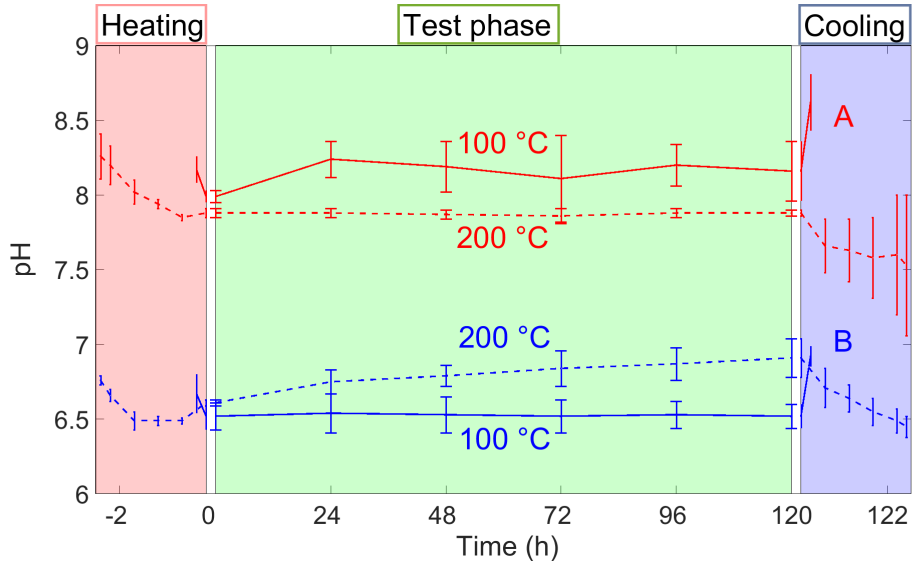

Figure 4. The pH evolution of fluids A or B in tests carried out up to either 100 or 200 °C. The error bars indicate the standard deviation from three individual experiments.

3.2. Open Circuit Potential (OCP) Evolution

The OCP of the metal sample was continuously monitored during the heating and cooling phases as well as during the intermediate test phase of five days. Figure 5 shows the OCP evolution obtained when solutions A and B were tested in the autoclave up to 100 or 200 °C. Here, it can be noticed that the measured OCP was generally higher during the cooling phase in all combinations. A reason for this could be that the time elapsed between the end of the heating phase and the beginning of the cooling phase was 5 days, which might be a reasonable time for the corrosion state of the sample to change. Furthermore, the tested low-alloyed steel (L80 Type 1) showed lower OCP values in fluid A than in fluid B, which is a more aggressive solution in terms of chlorides and pH.

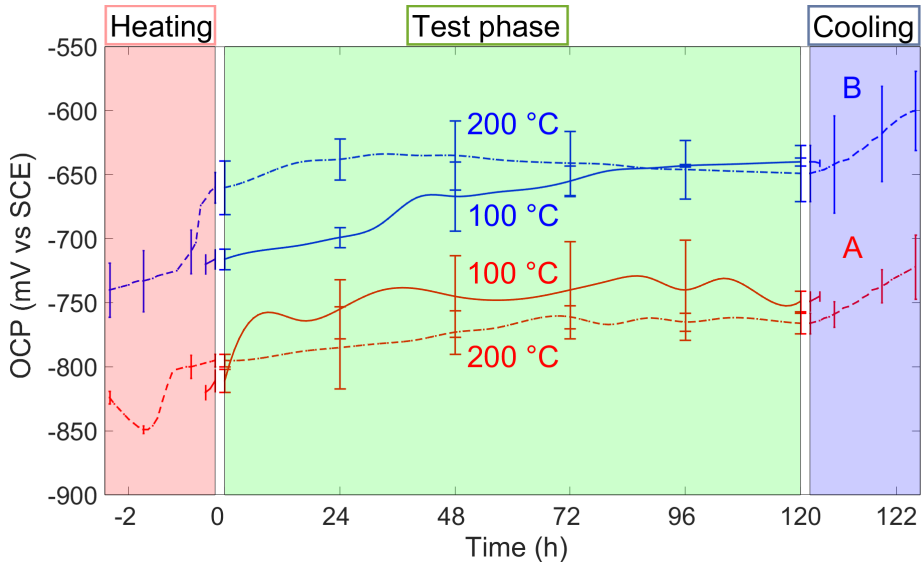

Figure 5. The open circuit potential (OCP) (mV vs Saturated Calomel Electrode, SCE) measured in the tests with fluids A and B at temperatures of either 100 or 200 °C. Each line indicates the average of three measurements and the error bars represent the standard deviation. The shown potentials were converted to the SCE scale, but they were measured with a high-temperature and high-pressure Ag/AgCl reference electrode.

3.3. Corrosion Rates

LPR measurements were carried out during the five day test phase at which the temperature was kept at 100 or 200 °C. This allowed us to calculate the corrosion rate of the metal sample over time, as shown in Figure 6. In all conditions, the instantaneous corrosion rates of the metal were generally below 100 µm/year, except in fluid B at 100 °C. In this case, a pronounced decrease over time was observed until a stable value was reached after approximately 80 h.

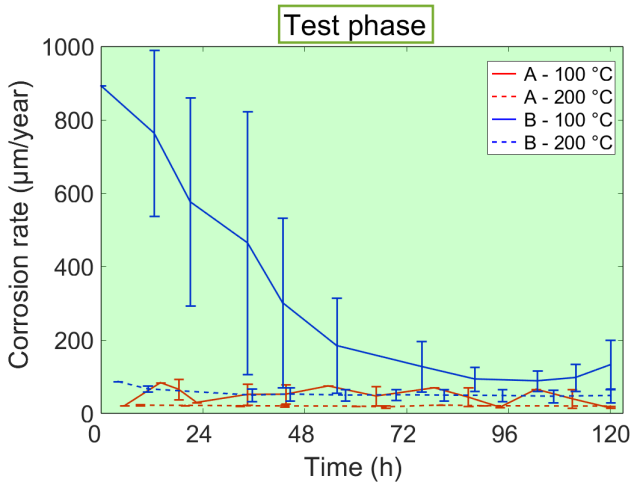

Figure 6. Instantaneous corrosion rates (µm/year) obtained from electrochemical measurements performed in fluids A and B at 100 or 200 °C. The values are the average of three individual measurements and the error bars indicate the standard deviation.

At 100 °C, the corrosion rates were also obtained from gravimetric tests. The comparison of the corrosion rates obtained applying both methods is reported in Table 4. The corrosion rates obtained from electrochemical tests were calculated by integrating the area under the curves in Figure 6 and dividing this by the duration of the test phase (namely, 120 h). This permits us to compare these values

to the corrosion rates obtained by gravimetry. Table 4 shows that the results obtained from the two methods are in overall agreement.

Table 4. Comparison of corrosion rates (averaged over time) obtained from electrochemical (linear polarization resistance (LPR) measurements) and gravimetric tests for the steel grade L80 Type 1 in fluids A and B at 100 °C.

Temperature	Fluid	Corrosion Rate (μm/year)	
		Gravimetric Tests (720 h)	Electrochemical Tests (120 h)
100 °C	A	92 ± 22	48 ± 11
	B	245 ± 43	308 ± 136
200 °C	A	-	19 ± 1
	B	-	52 ± 14

3.4. Surface and Fluid Analyses

Stereomicroscopy images of metal coupons that were tested in fluids A and B in gravimetric experiments at 100 °C are shown in Figure 7. The metal coupons exposed to fluid A revealed a thicker corrosion layer on the surface (Figure 7a), but with corrosion products that were easily detachable. Furthermore, certain parts of the metal surface were not completely covered with products, as can be seen in Figure 7b. On the other hand, the metal coupons exposed to fluid B showed more porous corrosion products, as shown in Figure 7c,d.

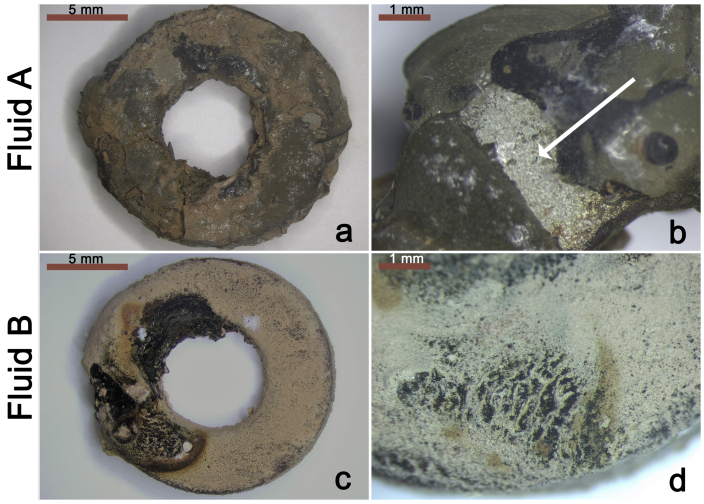

Figure 7. Steel coupons after gravimetric tests in fluids A and B at 100 °C. (**a**) General view of metal coupon after test in fluid A; (**b**) part of metal coupon (indicated by arrow) not covered with corrosion products after test in fluid A; (**c**) general view of metal coupon after test in fluid B; (**d**) porous corrosion products formed on the surface of a metal coupon during immersion in fluid B.

Furthermore, Figure 8 shows the surface appearance of the metal samples after exposure in the electrochemical cell to the synthetic fluids A or B at one of the two testing temperatures (100 or 200 °C). Figure 8a,b show the micromorphology of the corrosion products of the samples exposed to fluid A at 100 and 200 °C, respectively. Whereas the corrosion products formed at 100 °C present a cubic-shape morphology, the corrosion products formed on the metal surface at 200 °C mostly look like agglomerations of spherical particles. Moreover, the corrosion products of the metal samples exposed to fluid B at 100 and 200 °C show significantly different morphologies than those exposed to fluid A. For instance, at 100 °C, two types of corrosion products were formed on the metal surface

(Figure 8c): porous-rounded (P) and lamellar-cubic structures (L). At 200 °C, the corrosion products are scattered, not interconnected, and, in some cases, hollow deposits are visible (Figure 8d).

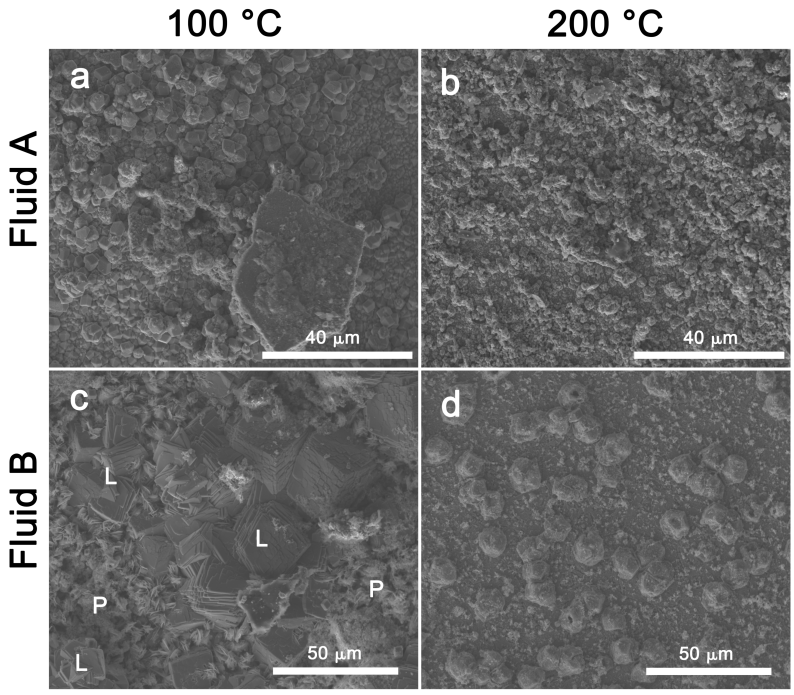

Figure 8. Scanning electron microscopy (SEM)-secondary electron (SE) micrographs of the samples surface after electrochemical experiments in different environments: (**a**) at 100 °C in fluid A; (**b**) at 200 °C in fluid A; (**c**) at 100 °C in fluid B (P and L refer to porous and lamellar corrosion products, respectively); (**d**) at 200 °C in fluid B.

In addition, XRD and EDX analyses indicated that magnetite (Fe_3O_4) and hematite (Fe_2O_3) were the main corrosion products deposited on the surface of the metal samples in contact with fluid A (at 100 and 200 °C) and fluid B at 200 °C.

The chemical analysis of the fluids by ICP-OES showed that the composition of both fluids slightly changed during the experiments at 100 and 200 °C, as can be seen in Figure 9a,b, respectively. For the tested solutions and temperatures, the most significant variations in concentration concern the elements Mg, Ca, K, and Fe, Mn, Cr. On the other hand, the chemical composition of the fluids measured by ICP-OES before the tests (Figure 9a,b) correspond accurately to the theoretical ones reported in Table 2.

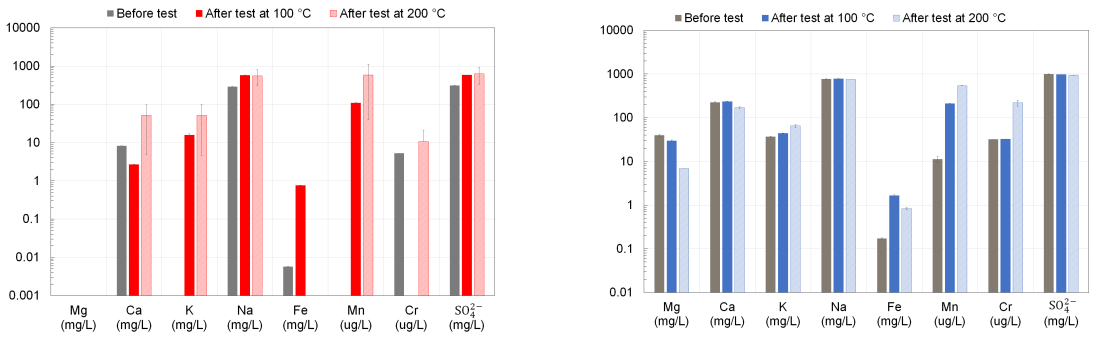

(**a**) (**b**)

Figure 9. Chemical composition of fluids A (**a**) and B (**b**) as measured by inductively coupled plasma optical emission spectroscopy (ICP-OES), before and after the tests carried out at 100 and 200 °C. The results are shown as the mean values of different experiments and their standard deviation.

4. Discussion

The measured open circuit potentials (Figure 5) were more positive than the reversible potential of the hydrogen evolution reaction. At 100 °C, the difference was approximately 100 mV, while at 200 °C, the difference was approximately 200 mV (independently of fluid type at both temperatures). Given the thermodynamic stability of iron compounds at high temperature and as a function of pH [54], the differences between the measured OCP and the reversible potential of the hydrogen evolution reaction indicate that the corrosion products precipitated on the sample surfaces were magnetite (at 100 °C) and magnetite/hematite (at 200 °C) (see Figure 10). This is in agreement with the results of the XRD and EDX analyses of the surfaces after the exposure tests (see Electronic Supplementary Materials).

At neutral pH and at 100 °C, the difference in reversible potentials of the iron dissolution and hydrogen evolution reactions is about 100 mV (see Figure 10a). Thus, the cathodic reaction promoting $Fe \rightarrow Fe^{2+} + 2e^{-}$ can be hydrogen evolution, and due to the high "driving voltage", high corrosion rates can occur. In addition, as oxygen was not completely removed from the fluid with the nitrogen purging, but reduced to a low concentration, it might have contributed to the corrosion rates, at least initially. Upon formation of $Fe(OH)_2$, hematite may be formed through various oxidation steps, among them the Schikorr-reaction [55].

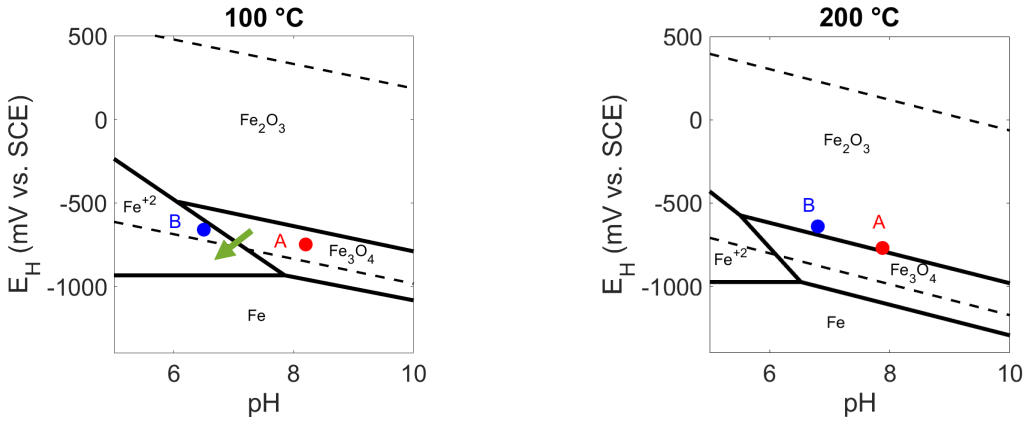

Figure 10. Pourbaix diagrams for iron at 10^{-6} m at 100 °C (**a**) and 200 °C (**b**), adapted from [54]. The red and blue points refer to fluids A and B, respectively. The green arrow shows the thermodynamic change of the system due to the increase of Fe^{2+} concentration.

Regarding the corrosion rates, it is interesting to note that in one case (fluid B, 100 °C) there was a marked change over exposure time, while this was not observed in the three other configurations (Figure 6). In the latter cases, the instantaneous corrosion rate was constantly below 100 µm/year, while in fluid B at 100 °C, the corrosion rate rapidly decreased from initially very high values (close to 1000 µm/year) to around 100 µm/year after approximately 80 h (three days). This is in agreement with theoretical reasoning based on the thermodynamic stability diagrams of iron at high temperature [54], which indicate that at pH values of approximately 7 (fluid B) there is active corrosion at 100 °C, while at 200 °C, hematite is stable (Figure 10). Thus, it can be reasoned that at 100 °C in fluid B, corrosion was rapidly occurring (considering also the supporting effect given by the lower pH and the presence of chlorides that may form soluble iron chloride complexes [56]). However, because of the massive precipitation of corrosion products, as evidenced by Figures 7 and 8, the electrochemical dissolution reactions became kinetically limited, which resulted in a decrease of the corrosion rate within a few days. We expect that the corrosion products precipitated due to an increase in Fe^{2+} concentration in the liquid. For instance, at a corrosion rate of 1000 µm/year within only a fraction of an hour, the Fe^{2+} concentration in the autoclave (electrolyte volume of approximately 1 L) would increase by one order of magnitude. Iron concentration increased indeed in the test solution during the test,

as evidenced by the ICP-OES measurements presented in Figure 9. This concentration change affects the thermodynamics of the system in such a way that at the given pH and potential (blue dot in Figure 10a), magnetite becomes stable. This may explain two observations: the rapid decrease of the corrosion rate (Figure 6) and the precipitation of corrosion scales, observed after the test (Figures 7 and 8). Although the corrosion rate for fluid B at 100 °C is relatively low at around 120 h, the long-term behaviour of the metal sample is difficult to predict. Of particular concern would be the pumping rate (namely, the rate at which new electrolyte enters the pipe from the rock). This rate of replenishing the electrolyte is critical as it determines to what extent the Fe^{2+} concentration can increase in the system. At high pumping rates, convection would limit the increase in Fe^{2+} concentration, which may keep the system in active corrosion conditions for longer terms than in our experiments.

In regard to the operation of a geothermal power plant, the steel grade API L80 shows better corrosion resistance at temperatures of 200 °C, which can be found nearby the bottom of the boreholes as shown in Figure 1, than those at 100 °C. This is because iron oxides are stable at 200 °C, leading to the formation of a protective scale [57]. However, the temperature in the reservoir might drop over the lifetime of the power plant [9], and, as a consequence, the entire system might be jeopardized. Furthermore, the chemical composition of the fluid might vary because of different reasons as, for example, the interaction with the reservoir rocks [36] or the periodic ingress of oxygen during maintenance activities of the power plant. In the former scenario, the pH might increase resulting in more favourable conditions for lower corrosion rates. In the latter, it is more challenging to predict the behaviour of the system.

5. Conclusions

The growing interest for the generation of electricity from geothermal resources makes investigations on the corrosion behaviour of metals particularly important. In this work, environmental conditions that are considered optimal for the generation of electricity in Switzerland have been successfully studied by various methods, such as electrochemical measurement techniques and gravimetric experiments. The potential corrosiveness of these geothermal fluids and their impact on the equipment of future geothermal power plants have been analyzed. Therefore, the outcome of this work will serve as a guideline for the selection of materials with regard to both costs and durability of the material.

Based on the current experimental observations, studying geothermal fluids representative for Northern Switzerland and the steel grade API L80 type 1, it can be concluded that higher temperatures (200 °C) lead to better corrosion resistance than lower temperatures (100 °C). Thus, equipment and installations located on the surface power plant will be more prone to corrosion. However, the corrosion rates obtained at higher temperatures, which are usually reached in the wells, can be considered negligible. While in constant conditions they are in the range 20–50 µm/year, which means technically acceptable sectional loss over the life time of a power plant, there is an uncertainty related to changes in solution chemistry and temperature during the operational life of a plant. A decrease in solution temperature or an increase in chloride concentration may shift the system and suddenly create more corrosive conditions, which considerably result in higher corrosion rates. Thus, further investigations on the protection provided by the corrosion products are necessary.

Supplementary Materials: The supplementary materials are available online at http://www.mdpi.com/2075-4701/9/3/331/s1.

Author Contributions: All authors designed the research. A.V.V. performed the experiments. All authors contributed in analysing the data and writing the paper. All authors read and approved the final manuscript.

Funding: The financial support of this project from the Swiss Competence Center for Energy Research–Supply of Electricity (SCCER-SoE) is kindly acknowledged.

Acknowledgments: The authors are also grateful to Asel María Aguilar Sanchez, Daniel Sanz Pont, and Sara Mantellato (IFB-ETH Zurich, Switzerland) for the help in using the SEM-EDX instrument, for the support in the elaboration of Figure 1, and for performing measurements by ICP-OES, respectively. We also thank Michael

Ploetze (IGT-ETH Zurich, Switzerland) for providing access to the XRD instrument and Marco May and Julien Millet (Vallourec, Aulnoye-Aymeries, France) for providing steel pipe sections.

Conflicts of Interest: The authors declare no conflict of interest.

References

1. Dickson, M.H.; Fanelli, M. *Geothermal Energy: Utilization and Technology*, 1st ed.; Routledge: London, UK, 2013; ISBN 978-18-4407-184-5.
2. Barbier, E. Geothermal energy technology and current status: An overview. *Renew. Sustain. Energy Rev.* **2002**, *6*, 3–65. [CrossRef]
3. Li, K.; Bian, H.; Liu, C.; Zhang, D.; Yang, Y. Comparison of geothermal with solar and wind power generation systems. *Renew. Sustain. Energy Rev.* **2015**, *42*, 1464–1474. [CrossRef]
4. Ellabban, O.; Abu-Rub, H.; Blaabjerg, F. Renewable energy resources: Current status, future prospects and their enabling technology. *Renew. Sustain. Energy Rev.* **2014**, *39*, 748–764. [CrossRef]
5. Fridleifsson, I.B.; Bertani, R.; Huenges, E.; Lund, J.W.; Ragnarsson, A.; Rybach, L. The possible role and contribution of geothermal energy to the mitigation of climate change. In Proceedings of the IPCC Scoping Meeting on Renewable Energy Sources, Luebeck, Germany, 20–25 January 2008; pp. 59–80.
6. Fridleifsson, I.B. Geothermal energy for the benefit of the people. *Renew. Sustain. Energy Rev.* **2001**, *5*, 299–312. [CrossRef]
7. Swiss Federal Office of Energy. Energy Strategy 2050 once the New Energy Act is in Force. Available online: http://www.bfe.admin.ch/energiestrategie2050/ (accessed on 3 January 2019).
8. Hirschberg, S.; Wiemer, S.; Burgherr, P. (Eds.) *Energy from the Earth: Deep Geothermal as a Resource for the Future?* vdf Hochschulverlag AG: Zurich, Switzerland, 2015; ISBN 978-3-7281-3654-1.
9. Olasolo, P.; Juárez, M.C.; Morales, M.P.; Liarte, I.A. Enhanced geothermal systems (EGS): A review. *Renew. Sustain. Energy Rev.* **2016**, *56*, 133–144. [CrossRef]
10. Wyss, R.; Link, K. Actual Developments in Deep Geothermal Energy in Switzerland. In Proceedings of the World Geothermal Congress 2015, Melbourne, Australia, 19–25 April 2015.
11. Link, K.; Rybach, L.; Imhasly, S.; Wyss, R. Geothermal Energy in Switzerland—Country Update. In Proceedings of the World Geothermal Congress 2015, Melbourne, Australia, 19–25 April 2015.
12. Genter, A.; Guillou-Frottier, L.; Feybesse, J.L.; Nicol, N.; Dezayes, C.; Schwartz, S. Typology of potential hot fractured rock resources in Europe. *Geothermics* **2003**, *32*, 701–710. [CrossRef]
13. Huenges, E. (Ed.) *Geothermal Energy Systems: Exploration, Development, and Utilization*; John Wiley and Sons: New York, NY, USA, 2010; ISBN 978-3-527-64461-2.
14. Tester, J.W.; Anderson, B.J.; Batchelor, A.S.; Blackwell, D.D.; DiPippo, R.; Drake, E.M.; Garnish, J.; Livesay, B.; Moore, M.C.; Nichols, K.; et al. *The Future of Geothermal Energy: Impact of Enhanced Geothermal Systems (EGS) on the United States in the 21st Century*; Massachusetts Institute of Technology: Cambridge, MA, USA, 2006; Volume 209.
15. Finger, J.; Blankenship, D. *Handbook of Best Practices for Geothermal Drilling*; Sandia National Laboratories: Albuquerque, NM, USA, 2010.
16. DiPippo, R. *Geothermal Power Plants: Principles, Applications, Case Studies and Environmental Impact*, 4th ed.; Butterworth-Heinemann: Oxford, UK, 2015; ISBN 978-00-8100-879-9.
17. Majer, E.L.; Baria, R.; Stark, M.; Oates, S.; Bommer, J.; Smith, B.; Asanuma, H. Induced seismicity associated with enhanced geothermal systems. *Geothermics* **2007**, *36*, 185–222. [CrossRef]
18. Evans, K.F.; Zappone, A.; Kraft, T.; Deichmann, N.; Moia, F. A survey of the induced seismic responses to fluid injection in geothermal and CO2 reservoirs in Europe. *Geothermics* **2012**, *41*, 30–54. [CrossRef]
19. Zang, A.; Oye, V.; Jousset, P.; Deichmann, N.; Gritto, R.; McGarr, A.; Majer, E.; Bruhn, D. Analysis of induced seismicity in geothermal reservoirs—An overview. *Geothermics* **2014**, *52*, 6–21. [CrossRef]
20. Mundhenk, N.; Huttenloch, P.; Sanjuan, B.; Kohl, T.; Steger, H.; Zorn, R. Corrosion and scaling as interrelated phenomena in an operating geothermal power plant. *Corros. Sci.* **2013**, *70*, 17–28. [CrossRef]
21. Karlsdóttir, S.N. Corrosion, scaling and material selection in geothermal power production. In *Comprehensive Renewable Energy*; Sayigh, A., Ed.; Elsevier: Amsterdam, The Netherlands, 2012; Volume 7, pp. 241–259. ISBN 978-0-08-087873-7.

22. Goldberg, A.; Owen, L.B. Pitting corrosion and scaling of carbon steels in geothermal brine. *Corrosion* **1979**, *35*, 114–124. [CrossRef]
23. Schreiber, S.; Lapanje, A.; Ramsak, P.; Breembroek, G. (Eds.) *Operational Issues in Geothermal Energy in Europe: Status and Overview*; Geothermal ERA NET: Reykjavik, Iceland, 2016; ISBN 978-9979-68-397-1.
24. Ellis, P.F.; Conover, M.F. *Materials Selection Guidelines for Geothermal Energy Utilization Systems*; Radian Corp.: Austin, TX, USA, 1981.
25. Iberl, P.; Alt, N.S.A.; Schluecker, E. Evaluation of corrosion of materials for application in geothermal systems in Central Europe. *Mater. Corros.* **2015**, *66*, 733–755. [CrossRef]
26. Frick, S.; Regenspurg, S.; Kranz, S.; Milsch, H.; Saadat, A.; Francke, H.; Brandt, W.; Huenges, E. Geochemical and process engineering challenges for geothermal power generation. *Chem. Ing. Tech.* **2011**, *83*, 2093–2104. [CrossRef]
27. Bertani, R. Geothermal power generation in the world 2010–2014 update report. *Geothermics* **2016**, *60*, 31–43. [CrossRef]
28. Regenspurg, S.; Wiersberg, T.; Brandt, W.; Huenges, E.; Saadat, A.; Schmidt, K.; Zimmermann, G. Geochemical properties of saline geothermal fluids from the in-situ geothermal laboratory Groß Schönebeck (Germany). *Chem. Erde-Geochem.* **2010**, *70*, 3–12. [CrossRef]
29. Mundhenk, N.; Huttenloch, P.; Kohl, T.; Steger, H.; Zorn, R. Metal corrosion in geothermal brine environments of the Upper Rhine graben – Laboratory and on-site studies. *Geothermics* **2013**, *46*, 14–21. [CrossRef]
30. Miranda-Herrera, C.; Sauceda, I.; González-Sánchez, J.; Acuña, N. Corrosion degradation of pipeline carbon steels subjected to geothermal plant conditions. *Anti-Corros. Methods Mater.* **2010**, *57*, 167–172. [CrossRef]
31. Karlsdóttir, S.N.; Hjaltason, S.M.; Ragnarsdottir, K.R. Corrosion behavior of materials in hydrogen sulfide abatement system at Hellisheiði geothermal power plant. *Geothermics* **2017**, *70*, 222–229. [CrossRef]
32. Klapper, H.S.; Bäßler, R.; Sobetzki, J.; Weidauer, K.; Stürzbecher, D. Corrosion resistance of different steel grades in the geothermal fluid of Molasse Basin. *Mater. Corros.* **2013**, *64*, 764–771. [CrossRef]
33. Czernichowski-Lauriol, I.; Fouillac, C. The chemistry of geothermal waters: its effects on exploitation. *Terra Nova* **1991**, *3*, 477–491. [CrossRef]
34. Nicholson, K. *Geothermal Fluids: Chemistry and Exploration Techniques*; Springer: Berlin/Heidelberg, Germany, 1993; ISBN 978-3-642-77846-9.
35. Breede, K.; Dzebisashvili, K.; Falcone, G. Overcoming challenges in the classification of deep geothermal potential. *Geother. Energy Sci.* **2015**, *3*, 19–39. [CrossRef]
36. André, L.; Rabemanana, V.; Vuataz, F.D. Influence of water–rock interactions on fracture permeability of the deep reservoir at Soultz-sous-Forêts, France. *Geothermics* **2006**, *35*, 507–531. [CrossRef]
37. Franco, A.; Villani, M. Optimal design of binary cycle power plants for water-dominated, medium-temperature geothermal fields. *Geothermics* **2009**, *38*, 379–391. [CrossRef]
38. Genter, A.; Evans, K.; Cuenot, N.; Fritsch, D.; Sanjuan, B. Contribution of the exploration of deep crystalline fractured reservoir of Soultz to the knowledge of enhanced geothermal systems (EGS). *C. R. Geosci.* **2010**, *342*, 502–516. [CrossRef]
39. Nogara, J.; Zarrouk, S.J. Corrosion in geothermal environment Part 2: Metals and alloys. *Renew. Sustain. Energy Rev.* **2018**, *82*, 1347–1363. [CrossRef]
40. Feili, H.R.; Akar, N.; Lotfizadeh, H.; Bairampour, M.; Nasiri, S. Risk analysis of geothermal power plants using Failure Modes and Effects Analysis (FMEA) technique. *Energy Convers. Manag.* **2013**, *72*, 69–76. [CrossRef]
41. Nogara, J.; Zarrouk, S.J. Corrosion in geothermal environment: Part 1: Fluids and their impact. *Renew. Sustain. Energy Rev.* **2018**, *82*, 1333–1346. [CrossRef]
42. Sonney, R.; Vuataz, F.D. Properties of geothermal fluids in Switzerland: A new interactive database. *Geothermics* **2008**, *37*, 496–509. [CrossRef]
43. Bodmer, P.; Rybach, L. Heat flow maps and deep ground water circulation: Examples from Switzerland. *J. Geodyn.* **1985**, *4*, 233–245. [CrossRef]
44. Breede, K.; Dzebisashvili, K.; Liu, X.; Falcone, G. A systematic review of enhanced (or engineered) geothermal systems: Past, present and future. *Geother. Energy* **2013**, *1*, 4. [CrossRef]
45. Medici, F.; Rybach, L. *Geothermal Map of Switzerland 1995 (Heat Flow Density)*; Commission Suisse de Géophysique: Zurich, Switzerland, 1995; No. 30.

46. CREGE (Centre de Recherche en Geothermie). BDFGeotherm—Web Database of Geothermal Fluids in Switzerland. Available online: https://crege.ch/index.php?menu=down&page=rd_BDFGeothem (accessed on 15 March 2016).
47. API Specification 5CT. *Specification for Casing and Tubing*, 8th ed.; API Publishing Services: Washington, DC, USA, 2005.
48. Vallejo Vitaller, A.; Angst, U.M.; Elsener, B. Setup of an electrochemical test cell for studying corrosion of steels for geothermal applications. Manuscript in preparation.
49. Stern, M.; Geary, A.L. Electrochemical polarization I. A theoretical analysis of the shape of polarization curves. *J. Electrochem. Soc.* **1957**, *104*, 56–63. [CrossRef]
50. Bard, A.J.; Faulkner, L.R. *Electrochemical Methods: Fundamentals and Applications*, 2nd ed.; John Wiley and Sons: New York, NY, USA, 2001; ISBN 978-0-471-04372-0.
51. Jones, D.A. *Principles and Prevention of Corrosion*, 2nd ed.; Prentice-Hall: Upper Saddle River, NJ, USA, 1996; pp. 143–167; ISBN 0-13-359993-0.
52. ASTM G31-12a. *Standard Guide for Laboratory Immersion Corrosion Testing of Metals*; ASTM International: West Conshohocken, PA, USA, 2012.
53. ASTM G 1-03. *Standard Practice for Preparing, Cleaning, and Evaluating Corrosion Test Specimens*; ASTM International: West Conshohocken, PA, USA, 2011.
54. Beverskog, B.; Puigdomenech, I. Revised Pourbaix diagrams for iron at 25–300 °C. *Corros. Sci.* **1996**, *38*, 2121–2135. [CrossRef]
55. Linnenbom, V.J. The Reaction between Iron and Water in the Absence of Oxygen. *J. Electrochem. Soc.* **1958**, *105*, 322–324. [CrossRef]
56. Tagirov, B.R.; Diakonov, I.I.; Devina, O.A.; Zotov, A.V. Standard ferric–ferrous potential and stability of FeCl to 90 °C. Thermodynamic properties of Fe (aq) 3+ and ferric-chloride species. *Chem. Geol.* **2000**, *162*, 193–219. [CrossRef]
57. Shannon, D.W. *Corrosion of Iron-Base Alloys Versus Alternate Materials in Geothermal Brines*; (Interim Report No. PNL-2456); Pacific Northwest Laboratories: Richland, WA, USA, 1977.